ATLAS Alignment, Tracking and Physics Performance Results

Giacinto Piacquadio[*][†]

ATLAS Collaboration
E-mail: `giacinto.piacquadio@cern.ch`

The present contribution describes the track reconstruction performance of the ATLAS Detector, based on the first proton-proton collisions delivered by the LHC accelerator at CERN at center-of-mass energies of 900 GeV and 7 TeV. The nominal tracking performance is first outlined in terms of expected track parameter resolutions and then the influence of the level of residual misalignment and of the precise knowledge of the detector material is discussed, based on real data. Preliminary results of methods which are sensitive to the amount of material in the tracking detector, as the reconstruction of photon conversions or the momentum scale and resolution of short-lived particles, are presented. The tracking performance in data and in simulation is compared and a quantitative estimate of the transverse impact parameter resolution, after unfolding the effect of the primary vertex resolution, is presented. Some information are finally provided about the physics performance of the tracking detector, in particular about the present phase of commissioning of the simplest *b*-tagging algorithms available in ATLAS, which are meant to be used for the first *top*-quark observation at $\sqrt{s} = 7$ TeV.

---

[*]Speaker.
[†]CERN

1. Introduction

The ATLAS experiment [1] started taking data from the proton-proton collisions delivered by the Large Hadron Collider (LHC) [2] at CERN at a centre-of-mass of 900 GeV in November 2009, while during 2010 data have been collected at an unprecedented centre-of-mass energy of 7 TeV. In order to achieve its physics goal the ATLAS experiment is equipped with several detectors, including an inner tracking device, the Inner Detector (ID), immersed in a 2 T solenoidal magnetic field, which provides a precise measurement of the momentum of charged particles.

The ID consists of three main detector subsystems: the Pixel detector, the Semiconductor Tracker (SCT) and the Transition Radiation Tracker (TRT) composed of drift tubes. The Pixel detector is the innermost subsystem and with its 1744 modules and 3 layers in the barrel plus 3 layers in each of the endcaps it provides two-dimensional point measurements. The single pixel size is $50 \times 400 \ \mu m$, which allows an intrisic resolution of $\approx 10 \ \mu$m in $r\phi$ and $\approx 115 \ \mu$m in z or R directions (parallel to the LHC beam in the barrel and radial in the endcaps). The SCT detector is composed of 4088 modules, 4 layers in the barrel and 9 layers in each of the endcaps, with each module having two pairs of single-sided silicon micro-strip sensors glued back-to-back with a relative stereo angle of 40 mrad. The resolution in $r\phi$ is $\approx 17 \ \mu$m, while the resolution in z in the barrel and in R in the endcaps is $\approx 580 \ \mu$m. The silicon detectors have a coverage of up to 2.5 in pseudorapidity. The momentum measurement of tracks is complemented by 30 hits on average in the TRT detector, which is composed of 4 mm wide straw tubes, with a coverage up to 2 in pseudorapidity and a resolution of $\approx 130 \ \mu$m per straw.

2. Tracking performance

2.1 Expected performance

The nominal tracking performance, as expected from studies performed with the Geant4 simulation of the ATLAS detector, has been described in Ref. [3].

The trajectory of a charged particle in ATLAS is conventionally expressed in terms of the perigee parameters of a helix, which define the track at the point of closest approach on the transverse plane to the primary interaction vertex. These parameters are the transverse and longitudinal distances of the track to the primary interaction vertex, respectively denoted d_0 and z_0, and the momentum vector, expressed in terms of azimuthal angle ϕ, polar angle θ and inverse momentum $1/p$. The transverse and longitudinal impact parameters are then defined as d_0 and $z_0 \times \sin\theta$. The expected resolution for the impact parameters and for the components of the momentum vector, representing the nominal tracking performance, can be parametrised, with some degree of approximation, with the following function:

$$\sigma_X(p_T) = \sigma_X(\infty) \left(1 \oplus \frac{p_X}{p_T} \right), \tag{2.1}$$

where $\sigma_X(\infty)$ is the asymptotic resolution expected at infinite momentum and p_X is a constant representing the value of p_T at which the multiple scattering contribution equals that from the detector resolution. Values for these parameters are shown in Table 1 for two different regions in pseudorapidity.

Track parameter	$0.25 < |\eta| < 0.50$		$1.50 < |\eta| < 1.75$	
	$\sigma_X(\infty)$	p_X (GeV)	$\sigma_X(\infty)$	p_X (GeV)
Inverse transverse momentum ($1/p_T$)	$0.34\,\text{TeV}^{-1}$	44	$0.41\,\text{TeV}^{-1}$	80
Azimuthal angle (ϕ)	$70\,\mu$rad	39	$92\,\mu$rad	49
Polar angle ($\cot\theta$)	0.7×10^{-3}	5.0	1.2×10^{-3}	10
Transverse impact parameter (d_0)	$10\,\mu$m	14	$12\,\mu$m	20
Longitudinal impact parameter ($z_0 \times \sin\theta$)	$91\,\mu$m	2.3	$71\,\mu$m	3.7

Table 1: Expected track parameter resolutions (RMS) at infinite transverse momentum, $\sigma_X(\infty)$, and transverse momentum, p_X, at which the multiple-scattering contribution equals that from the detector resolution. The values are shown for two η-regions, one in the barrel inner detector where the amount of material is close to its minimum and one in the endcap where the amount of material is close to its maximum. Taken from Ref. [3].

The expected asymptotic transverse and longitudinal impact parameter resolutions resemble well the intrinsic resolution of the Pixel detector in $r\phi$ and z ($\approx 10\,\mu$m in $r\phi$ and $\approx 115\,\mu$m in z).

The asymptotic track parameter resolutions can be significantly degraded by the effect of residual misalignments in the ID or, in particular for the momentum resolution, by the uncertainty in the mapping of the magnetic field. At low track p_T the correct computation of the track parameters requires a precise mapping of the material in the ID, due to the contribution of multiple scattering and of energy loss by ionisation.

2.2 Alignment

According to design specifications the effect of residual misalignments in the ID is expected to decrease the nominal performance expressed in terms of track parameter resolutions by less than 20% and the momentum scale is required to be correct within 0.1%.

The tools available for the alignment of the ID include the precision survey during assembly ($O(100\,\mu$m)), an optical hardware based monitoring, based on a Frequency Scanning Interferometry (FSI) system, which is able to monitor movements of the SCT structures in real time up to a precision of $O(1\,\mu$m), and the track-based alignment.

While the survey has been used for a first rough alignment of the ID, the track-based alignment is used as the main alignment tool. This makes use of the track-hit residuals, i.e. the distance from the extrapolated track position in a given detector module to the hit recorded in this module. The available algorithms try to reduce the squared sum of the residual significances[1] over a large number of reconstructed tracks: the global χ^2 minimisation algorithm, which tries to minimise this quantity while simultaneously performing a complete refit of the tracks with the updated module positions, has been the most widely used algorithm so far and is described in detail in Ref. [4]. The FSI system has not been integrated directly in the alignment procedure yet, but it was very helpful in confirming the remarkable mechanical stability of the SCT support structures.

A first *pre-collision* alignment has been carried out using the cosmic rays data collected in 2008, with the solenoidal magnetic field on and off, and was used for the reconstruction of the first collision data in November 2009. However, due to the limited statistics and due to the uneven

---

[1]The residual significance is defined as the residual divided by its error.

illumination of the ID by cosmic rays tracks, the alignment using cosmic rays is far from perfect, in particular in the endcap regions.

A first assessment of the tracking performance was also performed using cosmic rays, based on the *pre-collision* alignment, by splitting tracks from cosmic rays traversing the centre of the ID into two halves and determining their track parameter resolution as the width of their residual distributions divided by $\sqrt{2}$. The result for the transverse impact parameter resolution is shown in Fig. 1. Given the slightly different track selection criteria and different topology of these tracks (higher lateral displacement from the nominal interaction point with respect to collision events), the expected value of the asymptotic resolution for $p_T \to \infty$ for combined ID tracks is (14.3 ± 0.2) μm, while the measured resolution is (22 ± 1) μm. On the contrary, the measured longitudinal impact parameter resolution was (112 ± 4) μm, which is not far from the expected value of (101 ± 1) μm. These data point to a *pre-collision* residual misalignment in the barrel region of the pixel detector modules (which are most relevant for the impact parameter resolution) of the order of ≈ 20 μm in the $r\phi$ direction. The misalignment seems to be slightly smaller, of the order of ≈ 15 μm, for the pixel detector modules in the endcaps, due to the better mechanical stability and more precise positioning of these modules during assembly.
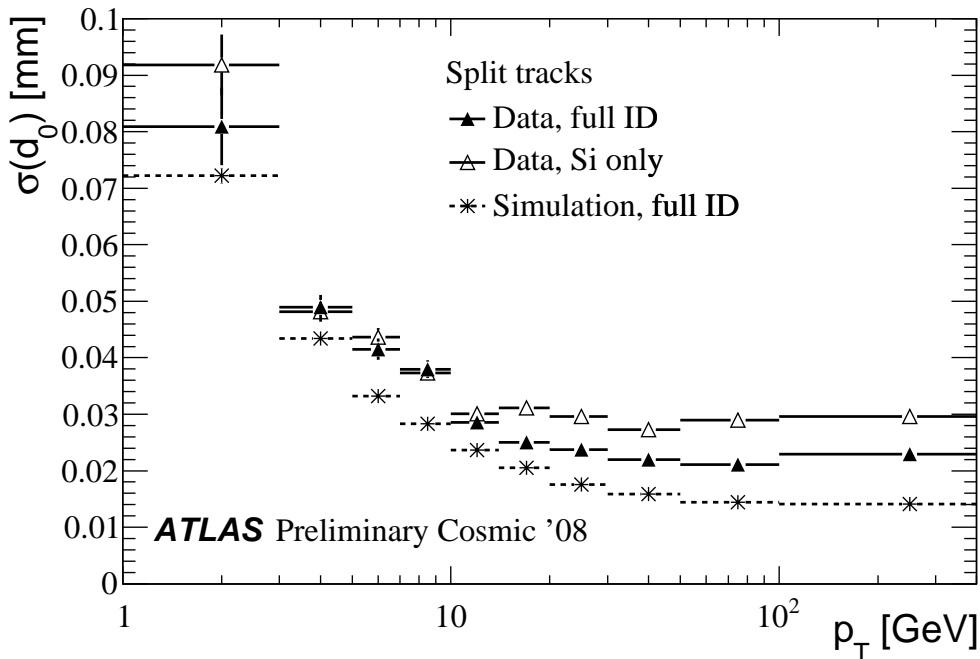

Figure 1: Transverse impact parameter resolution determined in cosmic rays using the half split tracks method, compared to the corresponding values obtained in Monte Carlo simulations with a perfectly aligned detector. Further details can be found in Ref. [5].

The alignment was significantly improved by the additional use of 900 GeV collision data, in particularly in the endcaps, where the alignment provided by cosmic rays was very poor. The new alignment configuration is defined here as *post-collision* alignment. The level of residual misalign-

ment in collision data was tested by analysing the unbiased[2] track-to-hit residuals averaged over all modules in the various sub-detectors, as shown in Fig. 2. Tracks were selected with transverse momentum above 2 GeV and at least 6 silicon hits.
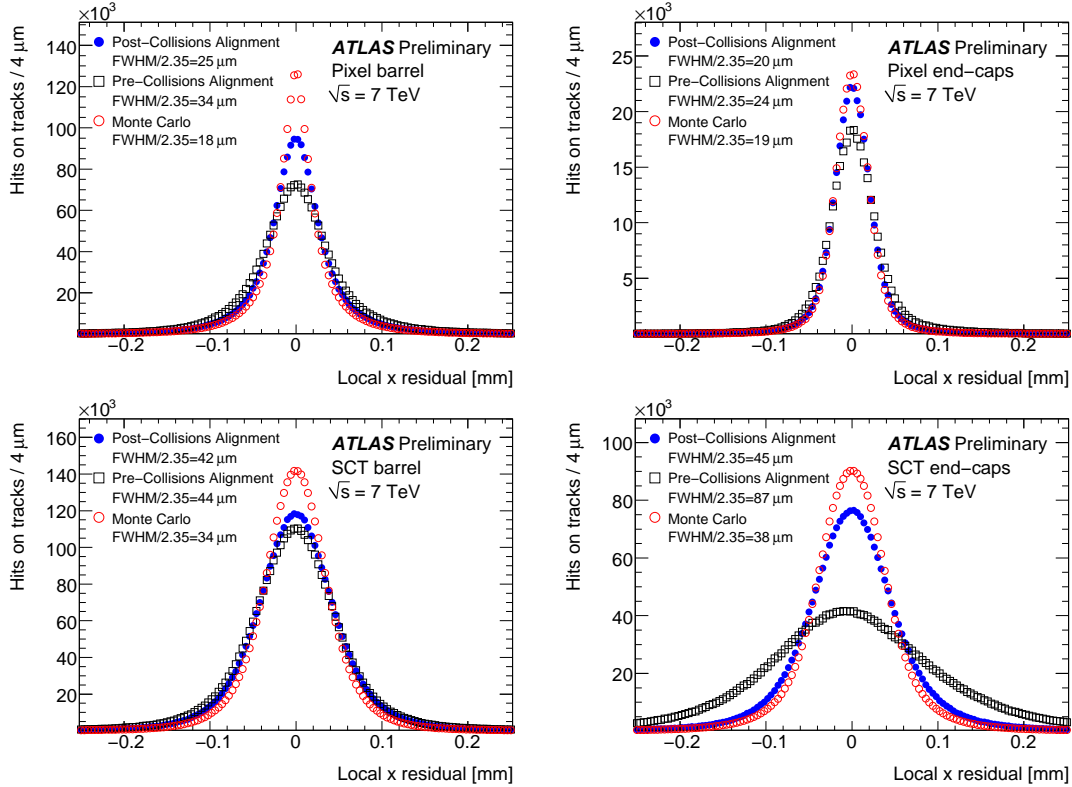

Figure 2: Local unbiased track-to-hit residuals in $r\phi$ for Pixel (top row) and SCT hits (bottom row), respectively for the barrel (left column) and for the endcaps (right column). Taken from Ref. [6].

In almost all cases a significant improvement in the residuals is seen when moving from the *pre-collision* to the *post-collision* alignment and a dramatic improvement is seen in the SCT end-caps, which were only very poorly illuminated by cosmic tracks.

The width of the track-to-hit residuals in the barrel part of the TRT detector (which was measured to be ≈ 141 μm, while ≈ 143 μm was expected) is already at the nominal value, while detailed work is ongoing to bring the measured width of residuals in the endcaps (≈ 162 μm) closer to the expected value (≈ 135 μm).

Assuming that the Monte Carlo simulation is correctly describing the intrinsic resolution of the Pixel and SCT detectors, the squared difference between the measured and nominal resolution can be interpreted as the contribution of residual misalignments of the ID to the track hit resolution, which is ≈ 17 μm in the Pixel barrel and ≈ 25 μm in the SCT barrel. More detailed information can be found in Ref. [6].

---

[2]The track is refitted after removing the hit under consideration

2.3 Mapping of material

In order to correctly describe the track uncertainty due to the effect of multiple scattering of charged particles in the detector material, of energy loss per ionisation and, in particular in the case of electrons, of bremsstrahlung, the simulation must correctly account for the amount, type and position of the material in the ID. This significantly affects the amount of energy which is deposited in the calorimeter, as well.

While a lot of effort has been put into an accurate control of the type and amount of material during the construction phase of the detector and in translating this into a realistic detector geometry to be used as input to the Geant 4 simulation, a precise mapping of the material detector using collision data is unavoidable to reach the precision required to match the ATLAS nominal performance specifications.

The first attempts in this direction rely on the following methods:

- Reconstruction of photon conversions as a function of radius R and pseudorapidity η

- Reconstruction of neutral Kaons using their most frequent decay channel $K_S \to \pi^+\pi^-$ and studying the dependence of their invariant mass distribution (central value and width) on the amount of material in the ID

- Reconstruction of hadronic interactions in the inner detector (not covered in the present Proceedings, see Ref. [7])

- Study of ϕ and η dependent occupancy in the calorimeter in minimum bias events (not covered in the present Proceedings, see Ref. [8])

2.3.1 Photon conversions

Photon conversion candidates are reconstructed starting from two tracks with transverse momenta above 0.5 GeV. In order to improve the selection purity the following requirements are made on the two candidate charged particles [9]:

- They have to be oppositely charged

- Selection criteria are applied on their distance (both in 2d and 3d) and on their opening angle

- They are both required to have at least 4 hits in the Pixel and SCT detectors

- They are required to be identified as electrons by using the particle identification provided by the Transition Radiation hits in the TRT

- They are required to form a vertex, where the two tracks are forced to have no opening angle, with a fit χ^2 smaller than 5 (corresponding to a χ^2 probability of more than $\approx 2.5\%$).

As a result of this selection, a complete tomography of the ATLAS detector can be obtained and compared to the analogous results in the simulation, as shown in Fig. 3. In particular the radial distributions of photon conversions already seems to show some small discrepancies between real data and simulation in some support structure of the SCT detector at a radial distance from the nominal center of the detector of around ≈ 20 and ≈ 25 cm.
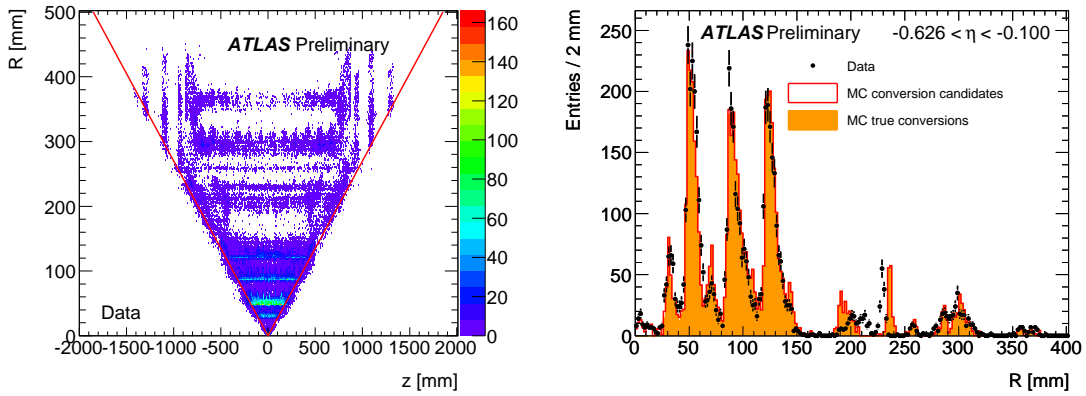
Figure 3:　　Map of photon conversion candidates in 7 TeV data in the *Rz* plane (left) and their radial distributions for a specific pseudorapidity region (right).

Given that that the cross section for a photon to convert into a pair of electrons is well known as a function of the radiation lengths of the traversed material, the fraction of converted photons can be translated directly into the radiation length of the material upstream.

$$\frac{X}{X_0} = -\frac{9}{7}\ln\left(1 - F_{conv}\right). \tag{2.2}$$

However, the measurement of the fraction of converted photons depends crucially on the conversion reconstruction efficiency. Work is ongoing to extract the efficiency to reconstruct photon conversions from data, which is an essential ingredient to get a handle on the systematic uncertainty associated with this measurement.

2.3.2 Reconstruction of neutral Kaons

Another very useful handle on the amount of material is provided by the reconstruction of K_S candidates starting from their $\pi^+\pi^-$ decay products and by requiring them to form a good vertex (Prob(χ^2)$> 0.01\%$), to have a transverse distance from the primary vertex above 4 mm and a small angle θ between the K_S candidate direction of flight and the momenta of both its decay products, with $\cos(\theta) > 0.999$. The invariant mass of those K_S candidates in data is shown in Fig. 5.

The K_S invariant mass peak occurs at 497.427 ± 0.006 MeV (error is only statistical), while the nominal PDG value is 497.614 ± 0.024 MeV [11]. The deviation from the PDG value is therefore 0.04%, which is not far from the nominal precision of the mapping of the magnetic field (0.02%). The Gaussian width is measured to be 5.60 MeV, while Monte Carlo simulations predict it to be 5.42 MeV. More details can be found in Ref. [10].

The peak position and the width of the K_S invariant mass peak are also very sensitive to the amount of material in the ID, while the sensitivity to residual misalignment should be low, since the average p_T of charged pions from K_S is around 0.4 GeV. This has been studied in 900 GeV data in Ref. [12]. A comparison of the K_S peak values as a function of detector radius between data and simulation in 900 GeV data is shown in Fig. 5. The deviations from simulation seen in data are well below 0.1% and are an indication that the average amount of material in the simulation is correctly described within a few percent.
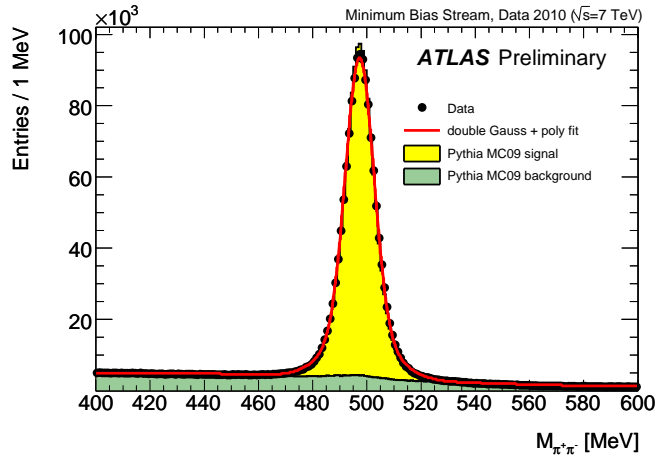
Figure 4: Invariant mass distribution for K_S candidates, compared to Monte Carlo prediction separately shown for the signal and the background components. Only candidates reconstructed in the barrel region of the tracking detector ($\eta < 1.2$) are shown here. Taken from Ref. [10].
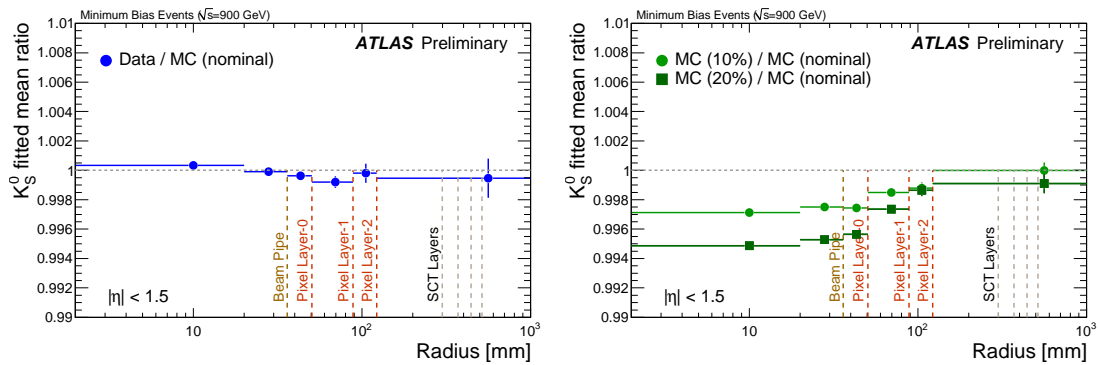

Figure 5: Peak value of the K_S invariant mass distribution as a function of detector radius, expressed as a ratio of data over simulation, on the left for the nominal ATLAS simulation and on the right for two set of simulated events, where 10% and 20% additional material has been included into the simulation in the ID.

2.4 Comparison of track related observables between data and simulation

In order to correctly describe the charged particles reconstruction efficiencies and related track parameter resolutions, the simulation needs to match the data with a high degree of accuracy. A first important check is whether the number of hits along a charged particle track in the Pixel and SCT detector are correctly described in the simulation. This is shown in Fig. 6 in minimum bias events for tracks passing the quality criteria required for the impact parameter based *b*-jet tagging algorithms. According to these criteria a track needs to have at least 7 silicon hits, with 2 hits in the Pixel detector and at least one of these in the innermost Pixel layer. In addition the transverse impact parameter $|d_0|$ is required to be smaller than 1 mm, the longitudinal impact parameter $|z_0 \times \sin(\theta)|$ is required to be smaller than 1.5 mm and the transverse momentum to be above 1 GeV.

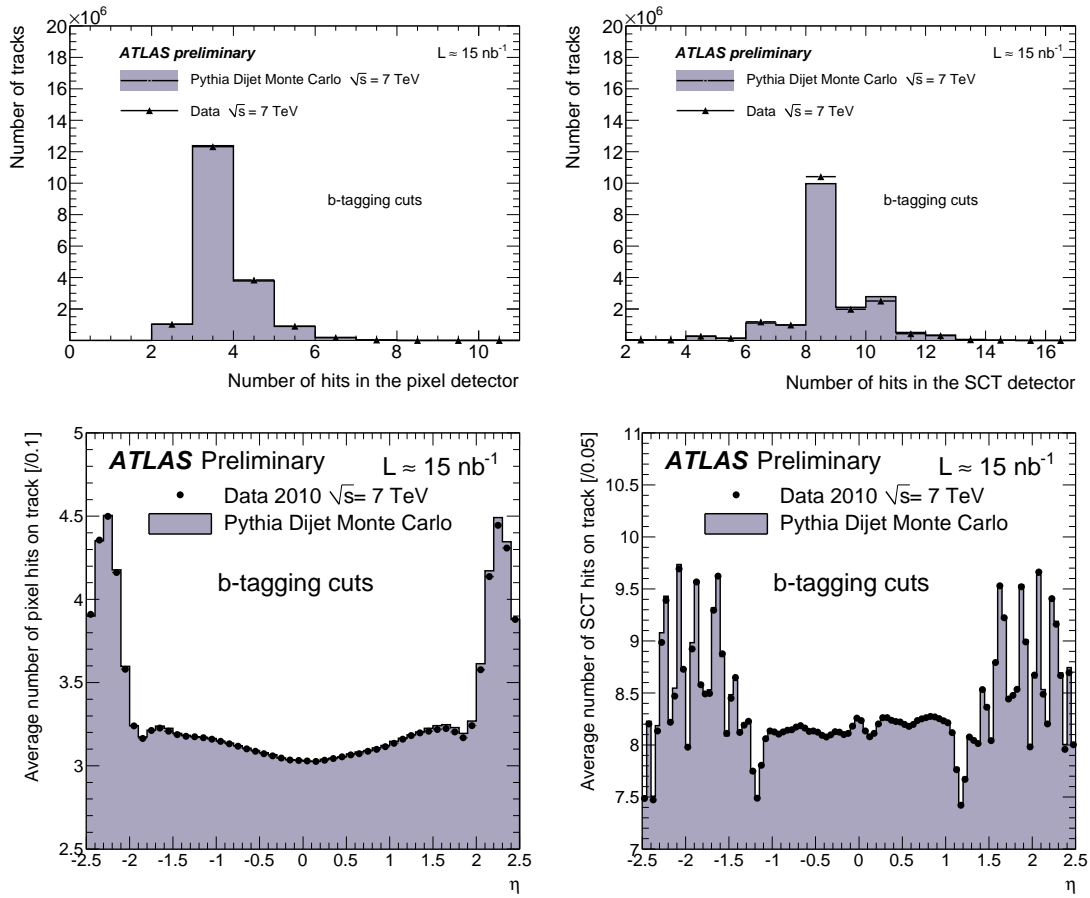The comparison between data and simulation shows that the hit patterns along a charged par-

Figure 6: Number of hits-on-track in the Pixel (left column) and the SCT detector (right column), first in absolute terms (top row) and then differentially as a function of pseudorapidity (bottom row). The data points are overlaid to the distributions expected from Monte Carlo simulation. Taken from Ref. [13].

ticle track in data are well reproduced by the Monte Carlo simulation.

Another distribution which is particularly sensitive to the efficiency of applying the *b*-tagging quality track selection and which has an important impact on the impact parameter resolution is the fraction of charged particle tracks with a hit in the innermost pixel Layer, which is shown in Fig. 7. Once hits corresponding to the few not operational Pixel modules are excluded, around 99.5% of the tracks turn out to have a hit in the innermost Pixel layer, with the fraction being slightly higher in data than in the simulation.

A comparison between data and simulation for the resulting transverse and longitudinal impact parameter distribution is shown in Fig. 8. The impact parameter distributions are slightly wider in data than in Monte Carlo, but one should keep in mind that the simulation is based on an ideally aligned detector geometry and therefore does not account for the effects of residual misalignment.
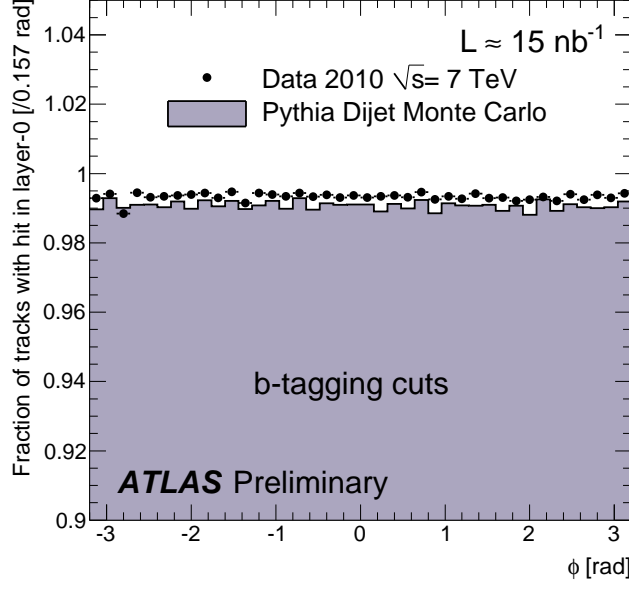
Figure 7: Fraction of tracks with a hit in the innermost Pixel layer. Details can be found in Ref. [13].

3. Primary vertex reconstruction

A primary vertex reconstruction algorithm is used to determine the position of the primary interaction vertex and of possible additional pile-up interactions taking place in the same bunch crossing. The vertex fit smoothly down-weights outliers, based on their track to vertex χ^2:

$$\chi^2 = \sum_{k=1}^{N} \omega_k \left(\chi_k^2 \right) \sum_i \left(\frac{\vec{r} - \vec{r}_k}{\vec{\sigma}_k}^2 \right)_i, \tag{3.1}$$

where the index i is summed over the number of tracks N used in the vertex fit and ω_k is a re-weighting factor which changes fit iteration after fit iteration and depends on the level of compatibility of the track to the present vertex position. The vertex fit is therefore robust against the presence of outliers from secondary interactions or additional pile-up events. Far outliers, compatible with the *beam-spot* on the transverse plane, are used to seed additional vertices. The procedure is iterated until all possible signal and pile-up vertices are found. The candidate signal vertex is selected as the vertex with the highest $\sum_i p_{T,i}^2$ of the tracks, where the index i corresponds to all tracks attached to a vertex. More details about the vertexing algorithm and a first study of the vertex performance, including an estimate of the vertex resolution in data in minimum bias events, can be found in Ref. [14].

The reconstructed primary vertices distribute according to the three-dimensional luminous region. The luminous region is periodically extracted through an unbinned likelihood fit, by deconvoluting the intrinsic primary vertex resolution on a vertex by vertex basis, as described in detail in Ref. [15] (Fig. 9). A careful monitoring of the vertex error is needed in order to make sure the
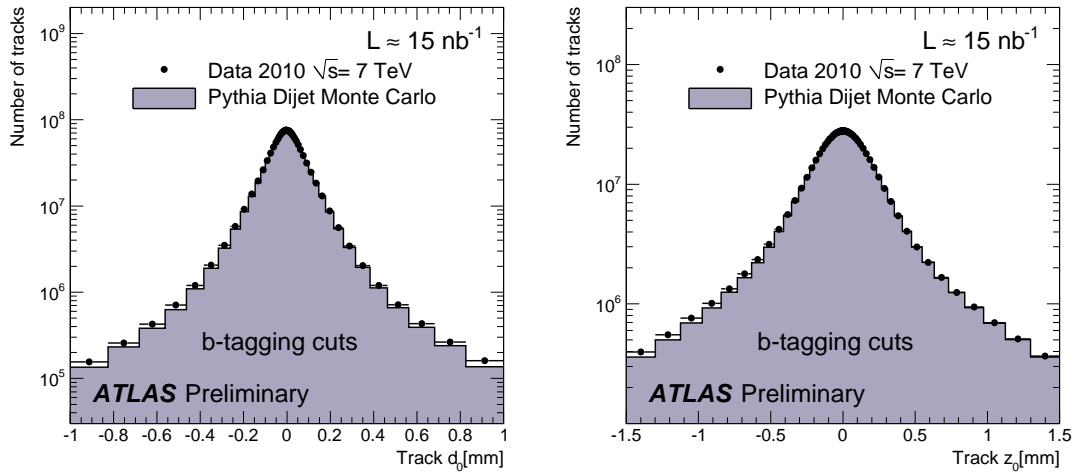
Figure 8: Distribution of transverse (left) and longitudinal (right) impact parameter for tracks passing the *b*-tagging quality selection.

deconvolution procedure is working properly. This can be obtained by the *vertex splitting* method, which has been studied both in Ref. [14] and Ref. [15].
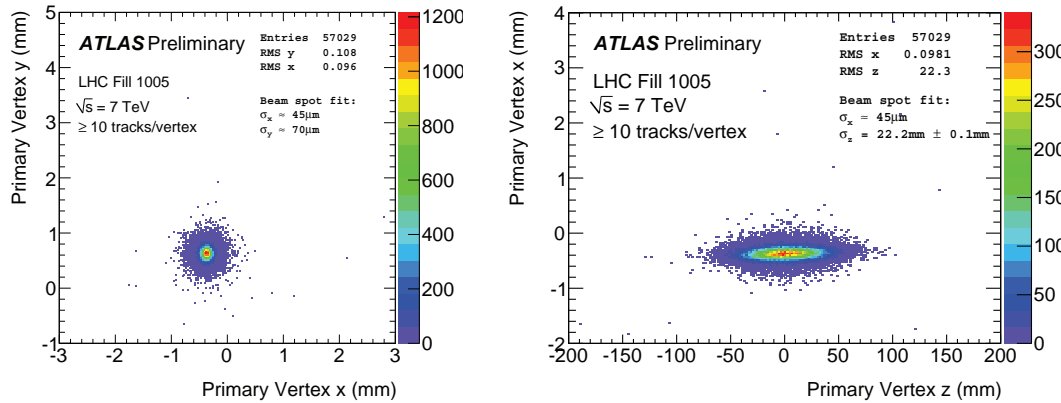

Figure 9: Primary vertex distributions in the *x-y* plane (left) and in the *x-z* plane (right) in 7 TeV data, uncorrected for the effect of finite resolutions. The resolution-corrected fit results are also shown on top. These data correspond to unsqueezed beam optics ($\beta^* = 11$ m). Only primary vertices with at least 10 tracks are selected. Taken from Ref. [15].

Once the luminous region is determined, it is used in the main reconstruction processing step as a constraint for the primary vertex reconstruction. This significantly improves the transverse resolution of the primary vertex, in particolar in soft events with no high p_T activity.

3.1 Measurement of impact parameter resolution

In Ref. [13] a method has been established to measure the impact parameter resolution di-

rectly in data, by considering only the core impact parameter resolution, to avoid the influence of charged particle tracks from secondary interactions, and by unfolding the effect of the primary vertex resolution, with respect to which the impact parameters are computed.

Given the limited amount of integrated luminosity available at the time of this study (15 nb^{-1}), the statistics allowed to measure the transverse impact parameter resolution up to transverse momenta of ≈ 15 GeV. The result in terms of unfolded transverse impact parameter resolution is shown in Fig. 10 for a specific pseudorapidity region corresponding to a part of the barrel region of the ID and is compared to Monte Carlo simulations.
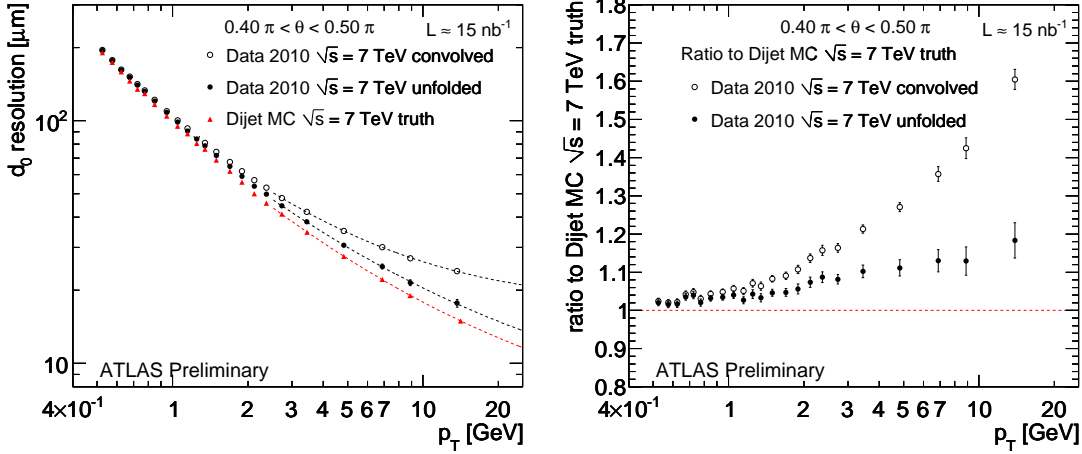

Figure 10: Unfolded transverse impact parameter resolution measured in data (full circles) as a function of p_T for values of the polar angle $0.40\pi < \theta < 0.50\pi$, compared to the expectations from Monte Carlo simulations (triangles). For reference, also the resolution before unfolding is shown (open circles). Taken from Ref. [13].

While at low transverse momenta, where the resolution is dominated by the effect of multiple scattering in the detector material, the agreement between data and simulation is at the few percent level, at higher transverse momenta the disagreement starts to be significant, reaching $\approx 15\%$ at $p_T = 15$ GeV. This is most probably due to the effect of residual misalignment of the ID, which is not taken into account in the simulation.

It would have been very interesting to extract the asymptotic resolution for $p_T \rightarrow \infty$ ($\sigma_{d_0}(\infty)$ of Eq. 2.1), i.e. the transverse impact parameter in the absence of any multiple scattering contribution, however no model was found to extrapolate in a realistic way the present data points to higher p_T values than those presently available. The model of Eq. 2.1 is not sufficiently accurate to allow for such an extrapolation. Therefore the data points around $p_T = 15$ GeV were used to select the region of the present p_T spectrum which is less sensitive to the effect of multiple scattering and most sensitive to the intrinsic detector resolution and effect of residual misalignments of the ID. The resulting transverse impact parameter resolutions at $p_T = 15$ GeV are shown in Fig. 11 and compared to the expected values from Monte Carlo simulations.

Assuming that the intrinsic detector resolution is correctly reproduced by the simulation, the difference between the measured and expected resolutions can be interpreted in terms of residual
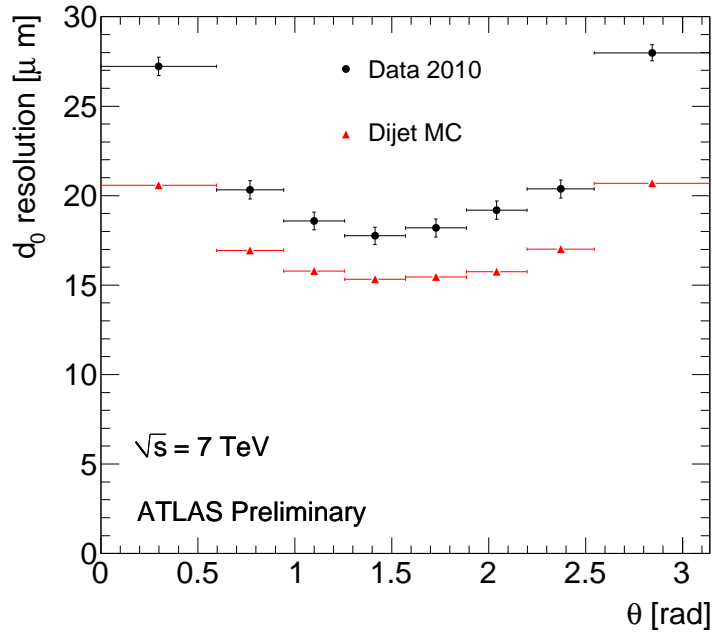
Figure 11: Unfolded impact parameter resolutions determined at p_T=15 GeV as a function of θ, compared to the expected resolutions from Monte Carlo simulation, assuming a perfectly aligned detector. Taken from Ref. [13].

misalignment of the ID. If interpreted in this way, the result points to a contribution of misalignment to the transverse impact parameter resolution of ≈ 10 μm in the barrel part, which is not far from ≈ 7 μm target corresponding to a degradation of the transverse impact parameter resolution of a perfectly aligned detector (10 μm, see Table 1) of less than 20%. At higher pseudorapidities the effect of the misalignment on the transverse impact parameter resolution increases up to $\approx$ 15-20 μm.

Already at this stage of the commissioning of the ID, the transverse impact parameter of tracks seems to be better constrained than the absolute position of the single Inner Detector modules (as described in Sec. 2.2), most probably thanks to the use of the *beam-spot constraint* during the alignment procedure, which constraints all primary tracks to pass through the *beam-spot* on the transverse plane during the alignment procedure. This constraint is less effective in the endcaps.

4. Reconstruction of cascade decays

During the first months of data taking similar studies as in the case of neutral Kaons decaying to pair of oppositely charged pions have been performed with more complex decay chain topologies, as the invariant mass distributions of D^*, Ω, Ξ and K^* candidates in Fig. 12 show. In most of the cases wrong-charge combinations of the decay products are used to estimate the level of combinatorial background from data: in most of the cases this estimate matches the invariant mass sidebands very well.

In all cases the fitted peak mass values agree with the nominal PDG values: as an example, the Ξ mass distribution peaks at $(1322.2 \pm 0.07(\text{stat.}))$ MeV as opposed to a nominal value of (1321.71 ± 0.07) MeV and the Ω mass distribution peaks at $(1672.8 \pm 0.3(\text{stat.}))$ MeV as opposed to a nominal value of (1672.45 ± 0.29) MeV. This again confirms the quality of the mapping of the magnetic field and of the estimate of energy loss per ionisation of charged particles while traversing the detector material.
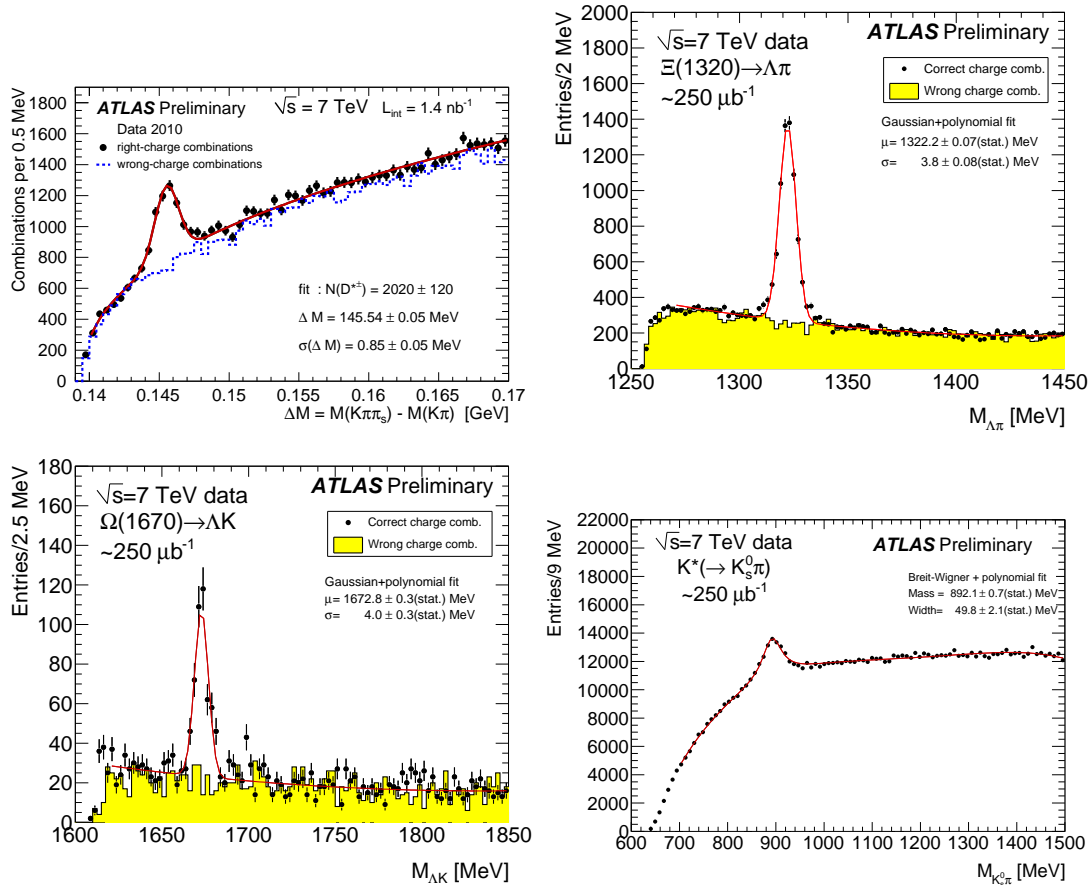

Figure 12: [top left] Distribution of mass difference between $K\pi$ and $K\pi\pi_s$ system, for the $D^{*\pm}$ candidates (decay chain: $D^{*+} \to D^0\pi_s^+ \to (K^-\pi^+)\pi_s^+$). [top right] Invariant mass of the Ξ candidates (decay chain: $\Xi \to \pi\Lambda \to \pi(p\pi)$). [bottom left] Invariant mass of the Ω candidates (decay chain: $\Omega \to K\Lambda \to K(p\pi)$). [bottom right] Invariant mass of the $K^*(890)$ candidates (decay chain: $K^* \to \pi K_S^0 \to \pi(\pi\pi)$). Taken from Refs. [16]-[17].

5. Early commissioning of the *b*-tagging algorithms

Since an early application of *b*-tagging to the *top*-quark analysis is planned, in order to improve the signal-to-background ratio and contribute to an earlier observation of the *top*-quark signal at $\sqrt{s} = 7$ TeV, the main focus at the moment is the commissioning of the simplest *b*-tagging algorithms available in ATLAS:

14

- *TrackCounting*, based on counting tracks with high *signed* transverse impact parameter significance;

- *JetProb*, relying on the resolution function for prompt tracks, where the probabilities for tracks in a jet to be prompt are combined into the probability for a jet to be a light-flavour jet (containing a *u*,*d*,*s* quark or gluon);

- a secondary vertex based algorithm, which relies on the explicit reconstruction of a secondary vertex and on its *signed* decay length significance.

The first two algorithms make only use of the transverse impact parameter significance of tracks ($S_{d_0} = d_0/\sigma(d_0)$). The *lifetime* sign is defined using the jet direction measured by the calorimeters: it is positive if the angle between the jet direction and the line joining the primary vertex to the point of closest approach is less than 90 degrees, while it is negative otherwise. Tracks from *b*- and *c*-hadron decays will have mostly positive lifetime signs, while prompt tracks will have randomly distributed lifetime signs.

5.1 Impact parameter based methods

The *TrackCounting* method is based on a simple cut on the three tracks with the highest impact parameter significance. A comparison of these three distributions between data and simulation is shown in Fig. 13. Apart from some differences in the core resolution, which was already pointed out in the present proceedings, 900 GeV data and Monte Carlo simulation agree fairly well over many orders of magnitude.

The *JetProb* algorithm is more sophisticated and is based on the determination of the resolution function $R(S_{d_0})$ for prompt tracks. This can be obtained in data from tracks with negative lifetime signs, which are mainly prompt tracks, and has been parametrised with the superposition of two Gaussians and two falling exponentials. The various components of this function are shown in Fig. 14.

In order to take the slightly different core resolution in data and simulation into account, the resolution function was separately determined in data and simulation and applied respectively to data and simulation. This allows for a comparison between data and simulation which takes this difference into account, since the effect expected due to the slightly different resolution on tracks with real lifetime from *b*- or *c*-decays is small.

The light-jet probability resulting from applying the *JetProb* algorithm on data and simulations is shown in Fig. 15. A good agreement is found, except for a small discrepancy at very low light-jet probability. However, a good agreement does not necessarily imply that the *b*-tagging efficiency for tagging *b*-jets and for rejecting light and *c*-jets is reproduced correctly in the simulation, since this depends also on whether the fraction of *b*, *c* and light-jets in minimum bias events are correctly predicted in the simulation.

5.2 Secondary vertex based methods

Using as input tracks matched to a jet, the secondary vertex based *b*-tagging algorithm looks for pairs of tracks compatible with a displaced vertex. Then all two-track vertices having an invariant mass compatible with the decay of a K^0_S or of a Λ particle or with a photon conversion
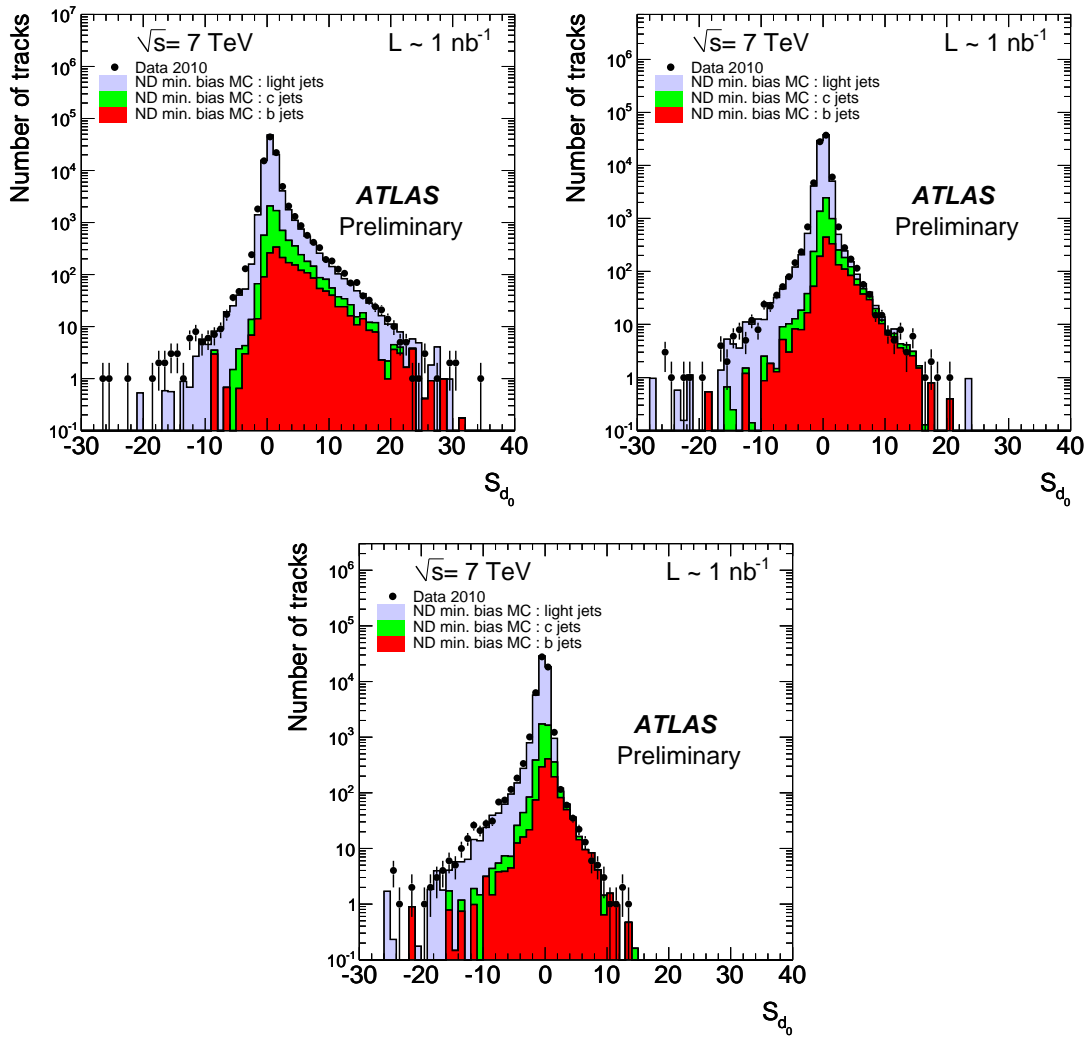
Figure 13: Distribution of the first (top left), second (top right) and third (bottom) highest impact parameter significance S_{d_0} for 900 GeV data (black points) and for simulation (plain histograms). Those distributions are used by the *TrackCounting* tagging algorithm. Taken from Ref. [18].

are not further considered. Two-track vertices corresponding to material interactions in the first Pixel layers are removed, as well. The remaining charged particle tracks are used to fit an inclusive secondary decay vertex, which in *b*-jets will mostly correspond to the inclusive *b*-/*c*-decay vertex.

After applying the secondary vertex *b*-tagging algorithm on minimum bias events in 7 TeV data and in simulation, the decay length significance distribution as shown in Fig. 16 is obtained. In this case, the agreement between data and simulation is not perfect: the reason for this might be the slightly different core resolution in data and simulation, which could particularly affect the fraction of mistagged light-jets.

Since the invariant mass of the charged particle tracks forming the secondary vertices is not used yet as an additional discriminator for improving the *b*-tagging performance, it is interesting to
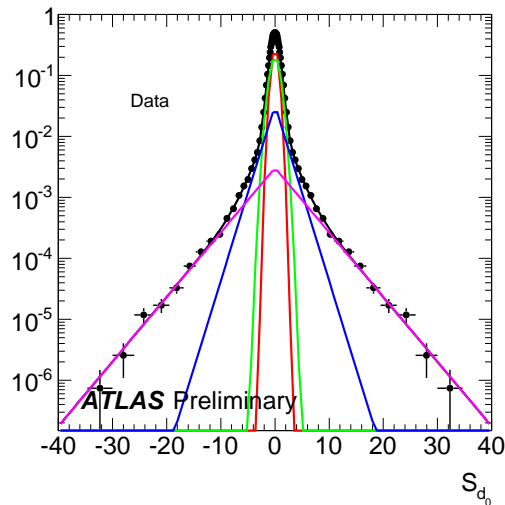
Figure 14: Distribution of the transverse impact parameter significance S_{d_0} of tracks for tracks with negative d_0 in 7 TeV data, symmetrised around $S_{d_0} = 0$ and fitted with the superposition of a double Gaussian and two falling exponentials. Taken from Ref. [18].

look at this distribution without and with a cut on the secondary vertex decay length significance. This is shown in Fig. 17. While the agreement in both cases is not perfect, the significant increase of the high vertex mass tail of the distribution after the cut on the decay length significance is a pretty convincing indication that real *b*-jets are indeed being selected here.

Further studies are ongoing both to determine the *b*-tagging efficiency and light-jet mistagging rates directly from data and to understand the remaining discrepancies between data and simulation.

6. Conclusions and outlook

The ATLAS Inner Tracking Detector is performing extremely well. The alignment of the Inner Detector has made significant progress with the use of 900 GeV collision data, allowing for track parameter resolutions to be obtained which are not too far from nominal expectations, and the higher amount of high p_T tracks which are already available in the currently collected 7 TeV data sample will allow to further improve the alignment precision.

The precise description of the material in the Inner Detector is crucial to correctly describe the tracking performance in data. The reconstruction of short-lived particles as K_S^0 shows that the momentum scale is close to nominal, pointing both to a good description of the average amount of material and to a very good quality of the magnetic field mapping. Methods are being developed to use photon conversions to measure the radiation lengths of the material in the Inner Detector as a function of the detector radius and pseudorapidity and work is ongoing to get a handle on the systematic uncertainty connected with the photon conversion reconstruction efficiency.

First tracking performance studies in 7 TeV data show a fair agreement between data and simulation. The hit efficiency in the various layers of the Pixel and SCT detectors seems to be correctly reproduced by the simulation. A more quantitative estimation of the transverse impact
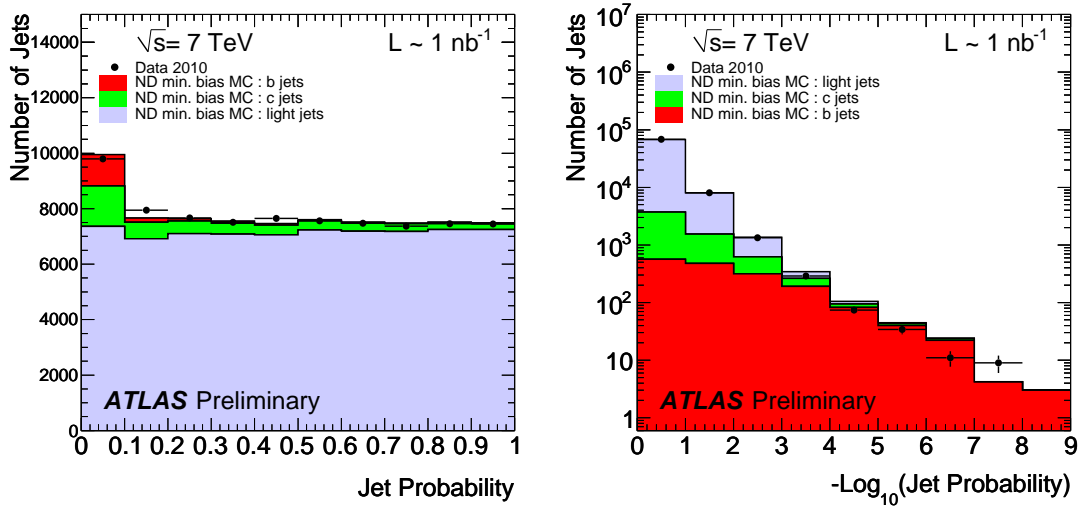
Figure 15: (left) Distribution of the probability P_{jet} for a jet to be compatible with a light jet, for real data (solid black points) and for simulated data (plain histograms). (right) Same distribution, but shown as the distribution of $-\log_{10}(P_{jet})$ for real data (solid black points) and for simulated data (plain histograms). Taken from Ref. [18].
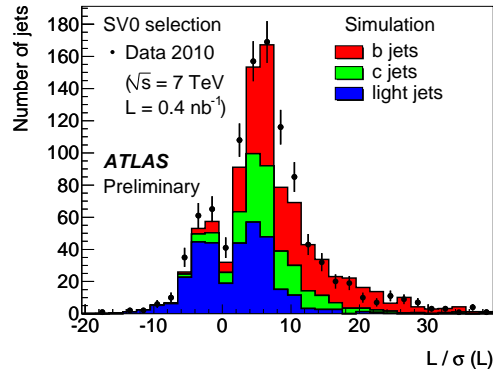

Figure 16: The three-dimensional decay length significance, signed with respect to the calorimeter jet axis, for all secondary vertices reconstructed in data events (markers). The expectation from simulated events (histogram) for non-diffractive minimum bias events, normalised to the number of jets in the data, is superimposed. Taken from Ref. [19].

parameter resolution shows that the resolution in data at low p_T, where the effect of multiple scattering is dominant, is within few percent from simulation, while at higher p_T the additional degradation due most probably to residual misalignment turns out to be $\approx 10\ \mu$m in the barrel and up to $\approx 20\ \mu$m in the endcaps.

First b-tagging studies in 7 TeV data show that the impact parameter tails due to the presence of secondary tracks not only from b and c-decays, but also from photon conversions, short-lived particles and material interactions are described fairly well in the simulation. The comparison
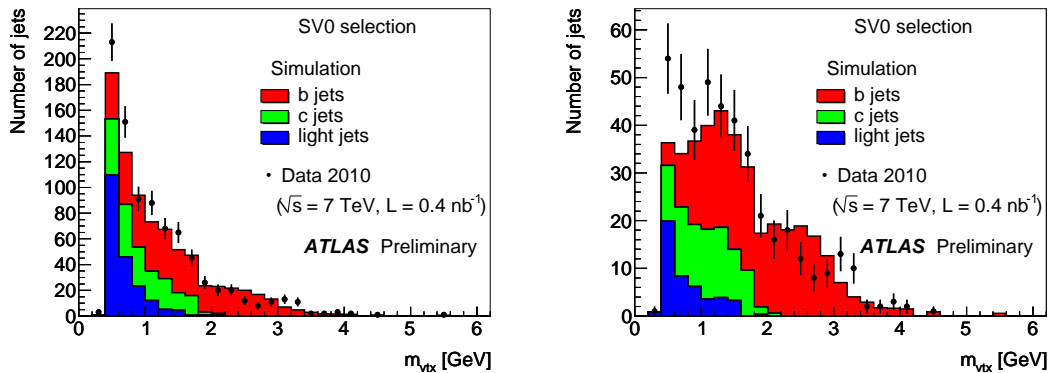
Figure 17: (left) The vertex mass distribution for all secondary vertices in data with positive decay length. The expectation from simulated events, normalised to the number of jets in the data, is superimposed. (right) Same distribution, but for all secondary vertices with decay length significance greater than 7.

between data and simulation for the discriminating variables of the simplest *b*-tagging algorithms available in ATLAS which are being commissioned right now looks promising, in particular for the *JetProb* algorithm. Work is ongoing to understand the origin of some discrepancies and the plan is to finish the commissioning of the simplest *b*-tagging algorithms and to measure their *b*-tagging efficiency and light-jet mistagging rates in data very soon, in order to contribute to the *top*-quark observation at $\sqrt{s} = 7$ TeV.

References

[1] The ATLAS Collaboration, *The ATLAS Experiment at the CERN Large Hadron Collider*, 2008, JINST **3** S08003

[2] Lyndon Evans and Philip Bryant (editors), *LHC Machine*, 2008, JINST **3** S08001

[3] The ATLAS Collaboration, *Expected Performance of the ATLAS Experiment - Detector, Trigger and Physics*, 2009, CERN-OPEN-2008-020 [hep-ph/0901.0512]

[4] P. Bruckman, A. Hicheur, S. Haywood, *Global χ^2 approach to the alignment of the ATLAS silicon tracking detectors*, ATLAS-INDET-PUB-2005-002

[5] Ryan, P. et al., *The ATLAS Inner Detector commissioning and calibration*, 2010 [hep-ph/1004.5293]

[6] The ATLAS Collaboration, *Alignment performance of the ATLAS Inner Detector Tracking System in 7 TeV proton-proton collisions at the LHC*, ATLAS-CONF-2010-067

[7] The ATLAS Collaboration, *Mapping the material in the ATLAS Inner Detector using secondary hadronic interactions in 7 TeV collisions*, ATLAS-CONF-2010-058

[8] The ATLAS Collaboration, *Probing the response of the ATLAS electromagnetic calorimeter and material upstream with energy flow from $\sqrt{s} =$7 TeV minimum bias events*, ATLAS-CONF-2010-037

[9] The ATLAS Collaboration, *Photon Conversions at $\sqrt{s} = 900$ GeV measured with the ATLAS Detector*, ATLAS-CONF-2010-007

[10] The ATLAS Collaboration, *Kinematic Distributions of K0s and Lambda decays in collision data at* $\sqrt{s} = 7\,TeV$, `ATLAS-CONF-2010-033`

[11] Amsler, C. et al., *Particle Data Group*, 2008, *Phys. Lett.* **B667**

[12] The ATLAS Collaboration, *Study of the Material Budget in the ATLAS Inner Detector with* K_S^0 *decays in collision data at* $\sqrt{s} = 900\,GeV$, `ATLAS-CONF-2010-019`

[13] The ATLAS Collaboration, *Tracking Studies for b-tagging with 7 TeV Collision Data with the ATLAS Detector*, `ATLAS-CONF-2010-070`

[14] The ATLAS Collaboration, *Performance of primary vertex reconstruction in proton-proton collisions at* $\sqrt{s} = 7\,TeV$ *in the ATLAS experiment*, `ATLAS-CONF-2010-069`

[15] The ATLAS Collaboration, *Characterization of Interaction-Point Beam Parameters Using the pp Event-Vertex Distribution Reconstructed in the ATLAS Detector at the LHC*, `ATLAS-CONF-2010-027`

[16] The ATLAS Collaboration, $D^{(*)}$ *mesons reconstruction in pp collisions at* $\sqrt{s} = 7\,TeV$, `ATLAS-CONF-2010-034`

[17] The ATLAS Collaboration, *Observation of* Ξ, Ω *baryons and* $K^*(890)$ *meson production at* $\sqrt{s} = 7\,TeV$, `ATLAS-CONF-2010-032`

[18] The ATLAS Collaboration, *Impact parameter based b-tagging algorithms in the 7 TeV collision data with the ATLAS detector: the Track Counting and JetProb algorithms*, `ATLAS-CONF-2010-041`

[19] The ATLAS Collaboration, *Performance of the ATLAS Secondary Vertex b-tagging Algorithm in 7 TeV Collision Data*, `ATLAS-CONF-2010-042`

20